

Interlayer coupling modulated tunable magnetic states in superlattice $\text{MnBi}_2\text{Te}_4(\text{Bi}_2\text{Te}_3)_n$ topological insulators

Jianfeng Guo,^{1,2,*} Huan Wang,^{1,2,*} Haoyan Zhang,^{1,2,*} Shuo Mi,^{1,2} Songyang Li,^{1,2} Haoyu Dong,^{1,2} Shiyu Zhu^{①,3}, Jiawei Hu,³ Xueyun Wang,⁴ Yanjun Li,⁵ Yasuhiro Sugawara,⁵ Rui Xu,^{1,2} Fei Pang^{②,1,2}, Wei Ji,^{1,2} Tianlong Xia,^{1,2,†} and Zhihai Cheng^{③,1,2,‡}

¹Key Laboratory of Quantum State Construction and Manipulation (Ministry of Education), Department of Physics, Renmin University of China, Beijing 100872, China

²Beijing Key Laboratory of Optoelectronic Functional Materials and Micro-nano Devices, Department of Physics, Renmin University of China, Beijing 100872, China

³Institute of Physics, Chinese Academy of Sciences, Beijing 100190, China

⁴School of Aerospace Engineering, Beijing Institute of Technology, Beijing 100081, China

⁵Department of Applied Physics, Graduate School of Engineering, Osaka University, Suita, Osaka 565-0871, Japan



(Received 7 October 2023; revised 11 March 2024; accepted 19 March 2024; published 4 April 2024)

The intrinsic superlattice magnetic topological insulators of $\text{MnBi}_2\text{Te}_4(\text{Bi}_2\text{Te}_3)_n$ ($n = 0, 1, 2, \dots$) provides a promising material platform for the realization of diverse exotic topological quantum states, such as quantum anomalous Hall effect and axion-insulator state. All these quantum states are sensitively dependent on the complex interplay and intertwinement of their band topology, magnetism, and defective structural details. Here, we report a comprehensive real-space investigation on the magnetic ordering states of $\text{MnBi}_2\text{Te}_4(\text{Bi}_2\text{Te}_3)_n$ using cryogenic magnetic force microscopy. The $\text{MnBi}_2\text{Te}_4(\text{Bi}_2\text{Te}_3)_n$ crystals exhibit a distinctive magnetic evolution from A-type antiferromagnetic to ferromagnetic states via the increased Bi_2Te_3 intercalation layers. The magnetic field- and temperature-dependent phase evolution behaviors of $\text{MnBi}_6\text{Te}_{10}$ and $\text{MnBi}_8\text{Te}_{13}$ are comparatively investigated to obtain the complete H - T phase diagrams. The combination impact of the intrinsic and defect-mediated interlayer coupling on their magnetic states were further discussed. Our results pave a possible way to realize more exotic quantum states via the tunable magnetic configurations in the artificial-stacking $\text{MnBi}_2\text{Te}_4(\text{Bi}_2\text{Te}_3)_n$ multilayers.

DOI: [10.1103/PhysRevB.109.165410](https://doi.org/10.1103/PhysRevB.109.165410)

I. INTRODUCTION

The interplay between magnetism and topology renders magnetic topological insulators (MTIs) an exceptional platform for investigating a diverse range of novel topological phenomena, including the quantum anomalous Hall effect (QAHE), axion insulators, and magnetic Weyl semimetals [1–5]. Recently, a van der Waals layered MnBi_2Te_4 (MBT) was proposed to be the first intrinsic stoichiometric antiferromagnetic (AFM) topological insulator [6–20]. Subsequently, nonmagnetic intercalation was employed as a material design strategy to modulate the magnetic state of the MBT. Therefore, natural superlattice structured $\text{MnBi}_2\text{Te}_4/(\text{Bi}_2\text{Te}_3)_n$ ($n = 1, 2, \dots$) are proposed whose interlayer coupling can be modulated by the intercalated Bi_2Te_3 (BT) layers [21–33]. The emergence of the tunable $\text{MnBi}_2\text{Te}_4/(\text{Bi}_2\text{Te}_3)_n$ family provides additional prospects for the development of MTIs.

The magnetism and topology of magnetic topological insulators are intrinsically intertwined, rendering the magnetically ordered state pivotal in determining their topological properties. For example, in MBT, the realization of the axion-

insulator state relies on its intrinsic AFM ground state [11], while achieving the QAHE requires polarization of its AFM ground state to a ferromagnetic (FM) state [10]. Therefore, the manipulation of its magnetic properties enables effective control over the topological state of the MTIs. For the $\text{MnBi}_2\text{Te}_4/(\text{Bi}_2\text{Te}_3)_n$ family, the interlayer AFM coupling of the MBT layer gradually decreases with increasing BT intercalation, enabling modulation of its magnetic properties. However, the increase of BT layers also engenders a concomitant augmentation in the intricacy of their magnetic properties, rendering them more elusive. For instance, MnBi_2Te_4 exhibits spin-flop transitions and canted AFM states [7,8], whereas MnBi_4Te_7 shows spin-flip transitions and FM and AFM coexisting states [22,24]. Furthermore, there is also potential in artificially designing and stacking thin flakes of $\text{MnBi}_2\text{Te}_4/(\text{Bi}_2\text{Te}_3)_n$ to achieve even more exotic topological states. Therefore, a detailed study of the magnetic properties of the $\text{MnBi}_2\text{Te}_4/(\text{Bi}_2\text{Te}_3)_n$ family is imperative to provide crucial insights for the realization of topological states. Although there have been reports on the magnetic properties of the $\text{MnBi}_2\text{Te}_4/(\text{Bi}_2\text{Te}_3)_n$ family, most of them pertain to macroscopic-scale measurements, while studies directly visualizing these properties at the microscopic scale remain relatively scarce.

In this work, we systematically characterize the $\text{MnBi}_2\text{Te}_4(\text{Bi}_2\text{Te}_3)_n$ family in real space using cryogenic

*These authors contributed equally to this work.

†Corresponding author: tlxia@ruc.edu.cn

‡Corresponding author: zhihaicheng@ruc.edu.cn

magnetic force microscopy (MFM) and concentrate on the magnetic properties of the weakly coupled $\text{MnBi}_6\text{Te}_{10}$ and $\text{MnBi}_8\text{Te}_{13}$. For $\text{MnBi}_6\text{Te}_{10}$, the intrinsic A-type AFM, surface spin-flip (SSF)+AFM, FM+SSF+AFM, and forced FM phases are sequentially realized via the increasing magnetic fields. For $\text{MnBi}_8\text{Te}_{13}$, the typical FM ground state and distinctive magnetic domain structures with potential topological properties are directly observed. Further temperature-dependent studies showed that the $\text{MnBi}_6\text{Te}_{10}$ and $\text{MnBi}_8\text{Te}_{13}$ demonstrate similar magnetic features near the phase transition temperatures, possibly related to the anisotropic-exchange-coupling-induced single-layer magnet (SLM) state [23]. The combination impact of the intrinsic and Mn_{Bi} -antisite-defect-mediated interlayer coupling on their magnetic states was further phenomenally discussed, and the configurable magnetic states for tunable exotic topological states in the artificial-stacking $\text{MnBi}_2\text{Te}_4(\text{Bi}_2\text{Te}_3)_n$ flakes are potentially proposed.

II. MATERIALS AND METHODS

A. Sample preparation

The $\text{MnBi}_{2n}\text{Te}_{3n+1}$ ($n = 1, 2, 3, 4$) single crystals were grown by the flux method [21]. Mn powder, Bi lump, and Te lump were weighed with the ratio of $\text{MnTe}:\text{Bi}_2\text{Te}_3 = 1 : 4$ (for $n = 1, 2, 3$) and $\text{MnTe} : \text{Bi}_2\text{Te}_3 = 19 : 81$ (for $n = 4$). The mixtures were loaded into a corundum crucible that was sealed into a quartz tube. Then the tube was put into a furnace and heated to 1100 °C for 20 h to allow sufficient homogenization. After a quick cooling to 605 °C at 5 °C/h, the mixtures were slowly cooled down to 590 °C (for $n = 1$), 585 °C (for $n = 2$), 581 °C (for $n = 3$), and 579 °C (for $n = 4$) at 0.5 °C/h and kept for 2 days. Finally, the single crystals were obtained after centrifuging. The platelike $\text{MnBi}_{2n}\text{Te}_{3n+1}$ single crystals with centimeter scale can be easily exfoliated. Although Bi_2Te_3 are inevitable coproducts, the $\text{MnBi}_{2n}\text{Te}_{3n+1}$ ($n = 1, 2, 3, 4$) single crystals can be identified by single-crystal x-ray diffraction. $\text{MnBi}_{2n}\text{Te}_{3n+1}$ ($n = 1, 2, 3, 4$) single crystals were cleaved in ambient conditions to expose fresh surfaces before MFM and scanning Kelvin probe force microscopy (SKPM) measurements were performed.

B. SKPM measurement

SKPM imaging was performed under ambient conditions by a commercial atomic force microscope (Park NX10) using a commercial electrostatic tip (Nanosensors, PPP-EFM). The single-pass mode was chosen to improve the spatial resolution of the surface potential. Topography and surface potential images can be obtained simultaneously, by applying two different frequencies of voltage to the probe. The scanning probe system operates at the resonant frequency (72 kHz) of the probe to obtain topographical images, while a voltage with a driving amplitude of 2.5 V and a frequency of 17 kHz is applied to the probe to obtain the surface potential image. The regions of MBT- and BT-termination surfaces can be distinguished by SKPM. By utilizing the MBT termination surface region as a reference in conjunction with the topography height profile, the stacking order of the $\text{MnBi}_2\text{Te}_4(\text{Bi}_2\text{Te}_3)_n$ family can be accurately and efficiently determined.

C. MFM measurement

The MFM experiments were conducted using a commercial magnetic force microscope (attoAFM I, attocube) employing a commercial magnetic tip (Nanosensors, PPP-MFMR; Quality factor ~ 1800 at 2 K) based on a closed-cycle He cryostat (attoDRY2100, attocube). The scanning probe system was operated at the resonance frequency, ~ 75 kHz, of the magnetic tip. The MFM images were captured in a constant height mode with the scanning plane nominally ~ 100 nm above the sample surface. The MFM signal, i.e., the change in the cantilever phase, was proportional to the out-of-plane stray field gradient. The dark (bright) regions in the MFM images represented attractive (repulsive) magnetization, where the magnetization was parallel (antiparallel) to the magnetic tip moments.

For $\text{MnBi}_6\text{Te}_{10}$, neglecting the magnetization contributed by AFM and domain walls, the normalized magnetization (M/M_S) can be reasonably estimated as a proportion of the FM phase in the MFM image. For $\text{MnBi}_8\text{Te}_{13}$, assuming that the FM-up and FM-down regions have the same magnetization, we can reasonably estimate the normalized magnetization (M/M_S) based on the area difference between the two regions. Therefore, the M - H curve can be deduced from the obtained MFM images.

D. Transport measurements

The measurements of magnetic property were performed on a Quantum Design magnetic property measurement system (MPMS-3).

III. RESULTS

In the natural superlattice structure $\text{MnBi}_2\text{Te}_4(\text{Bi}_2\text{Te}_3)_n$, the magnetic septuple layers (SLs; ~ 1.35 nm) of MBT are separated by n layers of nonmagnetic quintuple layers (QLs; ~ 1 nm) of BT, as schematically shown in Fig. 1(a). For $n \geq 1$, the members of the $\text{MnBi}_2\text{Te}_4(\text{Bi}_2\text{Te}_3)_n$ family have the presence of different cleaving ways between alternating MBT and nBT layers, resulting in MBT- or BT-terminated surfaces. The typical topography images of MnBi_2Te_4 [Fig. 1(b)], MnBi_4Te_7 [Fig. 1(d)], $\text{MnBi}_6\text{Te}_{10}$ [Fig. 1(f)], and $\text{MnBi}_8\text{Te}_{13}$ [Fig. 1(h)] are obtained by atomic force microscopy, while the layers of MBT and BT could not be readily resolved. Considering their different electronic properties, the corresponding surface potential images of MnBi_2Te_4 [Fig. 1(c)], MnBi_4Te_7 [Fig. 1(e)], $\text{MnBi}_6\text{Te}_{10}$ [Fig. 1(g)], and $\text{MnBi}_8\text{Te}_{13}$ [Fig. 1(i)] are further measured by SKPM [34].

The surface MBT (and BT) layers were clearly identified by their relatively low (and high) surface potentials in the SKPM images [32]. The difference in surface potential arises from the fact that MBT and BT possess distinct work functions (Supplemental Material Fig. S1 [35]). The greater the work function, the higher the surface potential difference (V_{CPD}). According to previous reports, the work function of MBT is 4.4 eV [36], whereas that of BT is 5.3 eV [37]. As a result, BT have a higher V_{CPD} compared to MBT. The proposed method enables the visual determination of the surface termination layer type in $\text{MnBi}_2\text{Te}_4(\text{Bi}_2\text{Te}_3)_n$, thereby facilitating accurate confirmation of the stacking order when combined

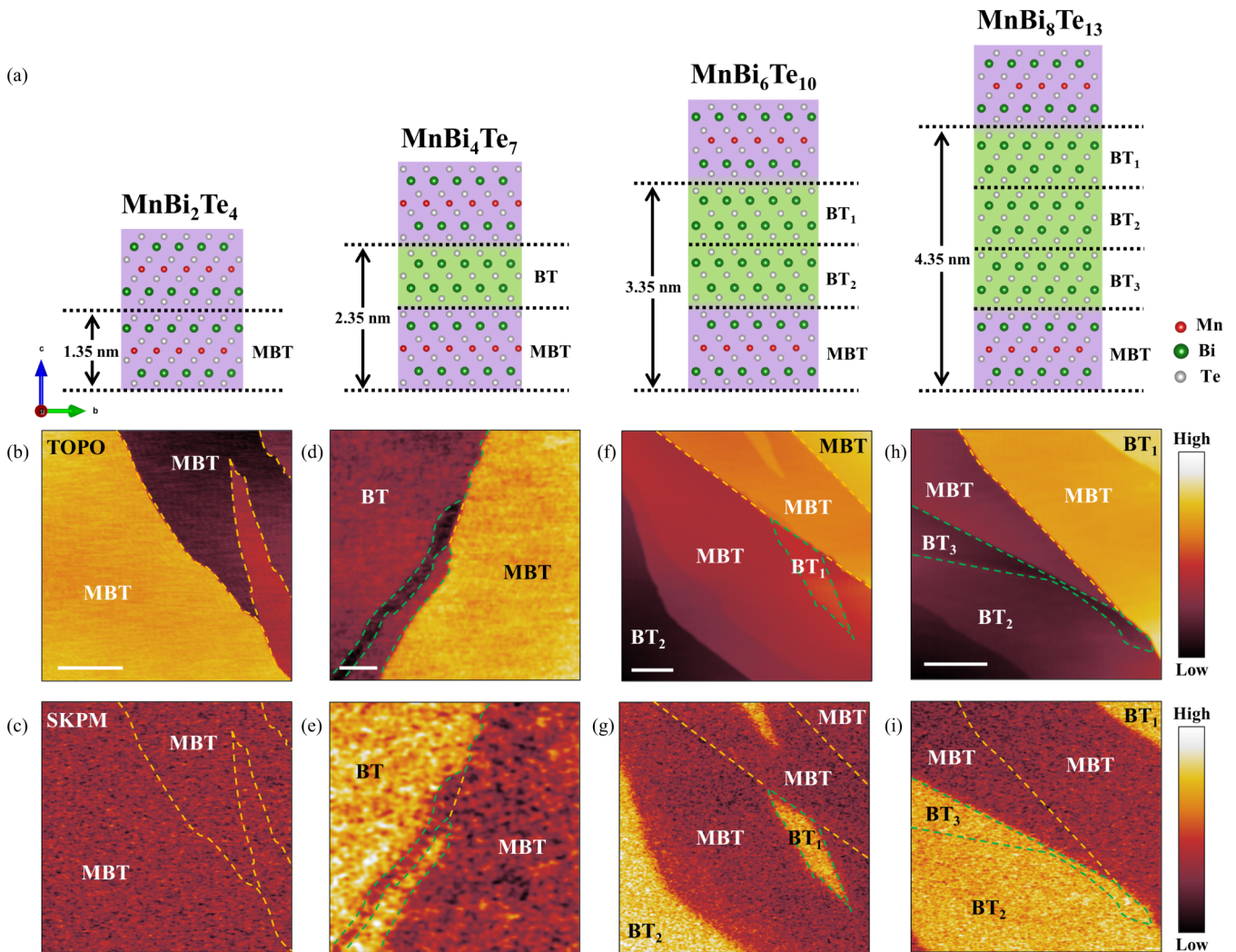


FIG. 1. Crystal structure and atomic force microscopy characterizations of the superlattice magnetic topological insulators $\text{MnBi}_2\text{Te}_4(\text{Bi}_2\text{Te}_3)_n$ single crystal. (a) Schematic illustrations of the crystal structures of MnBi_2Te_4 , MnBi_4Te_7 , $\text{MnBi}_6\text{Te}_{10}$, and $\text{MnBi}_8\text{Te}_{13}$. (b),(d),(f),(h) Atomic force microscopy topography images of MnBi_2Te_4 , MnBi_4Te_7 , $\text{MnBi}_6\text{Te}_{10}$, and $\text{MnBi}_8\text{Te}_{13}$. (c),(e),(g),(i) Corresponding surface potential images of (b), (d), (f), and (h) taken by scanning Kelvin probe microscopy (SKPM). Scale bar: 2 μm .

with topography height profiles (Fig. S2). Therefore, this approach could be extended to determine in detail the structural configurations of artificial-stacking MBT-BT multilayers in future investigations.

The superlattice topological insulators of $\text{MnBi}_2\text{Te}_4(\text{Bi}_2\text{Te}_3)_n$ consist of alternating magnetic MBT layers and the nonmagnetic nBT layers, in which the MBT layers hold substantial intralayer FM magnetic exchange coupling with the easy axis along the *c* axis. The A-type AFM states of $\text{MnBi}_2\text{Te}_4(\text{Bi}_2\text{Te}_3)_n$ have been theoretically predicted due to the interlayer AFM exchange coupling between the MBT layers through the nBT layers [7]. For MnBi_2Te_4 , it undergoes a spin-flop transition due to the combined influence of interlayer coupling energy and anisotropy energy. In contrast, for MnBi_4Te_7 , the reduction in interlayer coupling energy enables the dominance of anisotropic energy, resulting in a spin-flip transition instead of spin-canted behavior.

As the interlayer coupling energy is further reduced, the magnetic properties of the $\text{MnBi}_6\text{Te}_{10}$ should approach those

of a single layer. The previously reported theoretical and macroscopic transport results indicate that each MBT layer of $\text{MnBi}_8\text{Te}_{13}$ becomes an independent two-dimensional (2D) ferromagnet with negligible interlayer coupling, resulting in an SLM state without long-range order along the crystalline *c* axis [23]. The validity of this result on the microscopic real-space scale, however, requires further experimental validation. Furthermore, considering the magnetic sensitivity of many topological states [10,11], it is interesting and necessary to further investigate the interlayer coupling modulated tunable magnetic states in the $\text{MnBi}_2\text{Te}_4(\text{Bi}_2\text{Te}_3)_n$. In addition to the macroscopic magnetic measurements, the microscopic real-space characterizations of their tunable magnetic states using cryogenic MFM can enhance our understanding of these structure-sensitive magnetic phases and their coupling to topological states.

Figures 2(a)–2(d) and 2(e)–2(g) show typical MFM images and magnetic moment configurations for the magnetic ground state of the $\text{MnBi}_2\text{Te}_4(\text{Bi}_2\text{Te}_3)_n$ family at 1.7 K after zero-field cooling. For $n = 0, 1, 2$, all of them exhibit the

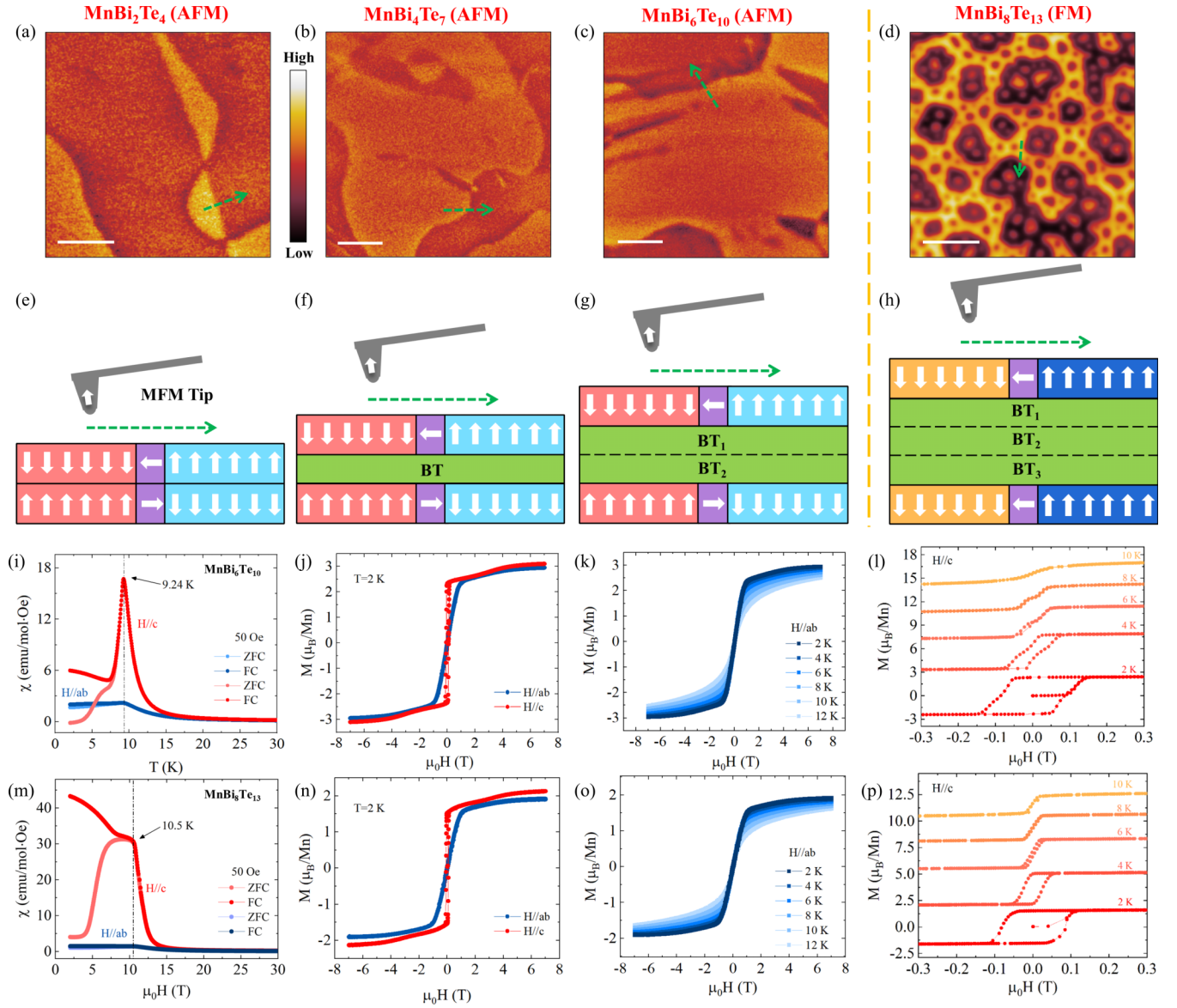


FIG. 2. MFM and transport characterizations of the superlattice $\text{MnBi}_2\text{Te}_4(\text{Bi}_2\text{Te}_3)_n$ single crystal. (a)–(d) Typical MFM images of $\text{MnBi}_2\text{Te}_4(\text{Bi}_2\text{Te}_3)_n$ single crystals at 1.7 K. Scale bar: 4 μm . (e)–(h) Schematic spin configurations for the magnetic states of $\text{MnBi}_2\text{Te}_4(\text{Bi}_2\text{Te}_3)_n$ along the green dashed lines marked in (a)–(d), where the magnetic layers MnBi_2Te_4 are separated by n layers of Bi_2Te_3 as interlayer spacers. (i), (m) Temperature dependence of zero-field-cooled (ZFC) and field-cooled (FC) magnetic susceptibility for (i) $\text{MnBi}_6\text{Te}_{10}$ and (m) $\text{MnBi}_8\text{Te}_{13}$. (j), (n) Field-dependent magnetizations (M - H) along $H||c$ and $H||ab$ at 2 K for (j) $\text{MnBi}_6\text{Te}_{10}$ and (n) $\text{MnBi}_8\text{Te}_{13}$. (k), (o) The M - H curves at different temperatures with $H||ab$ for (k) $\text{MnBi}_6\text{Te}_{10}$ and (o) $\text{MnBi}_8\text{Te}_{13}$. (l), (p) Enlarged M - H curves with $H||c$ for (l) $\text{MnBi}_6\text{Te}_{10}$ and (p) $\text{MnBi}_8\text{Te}_{13}$.

intrinsic A-type AFM ground states, which are characterized by two AFM domain states ($\uparrow\downarrow\uparrow\downarrow$ or $\downarrow\uparrow\downarrow\uparrow$) [19,20]. The relatively weak MFM signal difference (0.1°) between the two AFM domains arises from the respective attractive and repulsive interactions between the MFM tip and the topmost MBT layer with parallel and antiparallel magnetic moments, as schematically shown in Figs. 2(e)–2(g); while for $n = 3$, the $\text{MnBi}_8\text{Te}_{13}$ exhibits the FM state with relatively strong MFM signal contrast (14.1°) between the spin-up and spin-down domains, as shown in Figs. 2(d) and 2(h), and Fig. S3. It is unexpected that the gradually reduced interlayer coupling could be transformed from AFM to FM via the increased nBT layers, and no signatures or features of SLM were observed

at the ground state at 1.7 K. The result contradicts the theory. In fact, the FM coupling in $\text{MnBi}_8\text{Te}_{13}$ is attributed to MnBi antisite defects, which will be explained in detail in the Discussion section.

The impact of the gradually reduced interlayer coupling on the magnetic properties of the $\text{MnBi}_2\text{Te}_4(\text{Bi}_2\text{Te}_3)_n$ family were further discussed based on the macroscopic magnetic characterizations of $\text{MnBi}_6\text{Te}_{10}$ and $\text{MnBi}_8\text{Te}_{13}$. Their zero-field-cooled (ZFC) and field-cooled (FC) magnetic susceptibilities were comparatively measured and shown in Figs. 2(i) and 2(m). For $\text{MnBi}_6\text{Te}_{10}$, a sharp cusp feature is observed at ~ 9.24 K, similar to MnBi_2Te_4 and MnBi_4Te_7 , indicating an AFM transition; while, for $\text{MnBi}_8\text{Te}_{13}$, a large

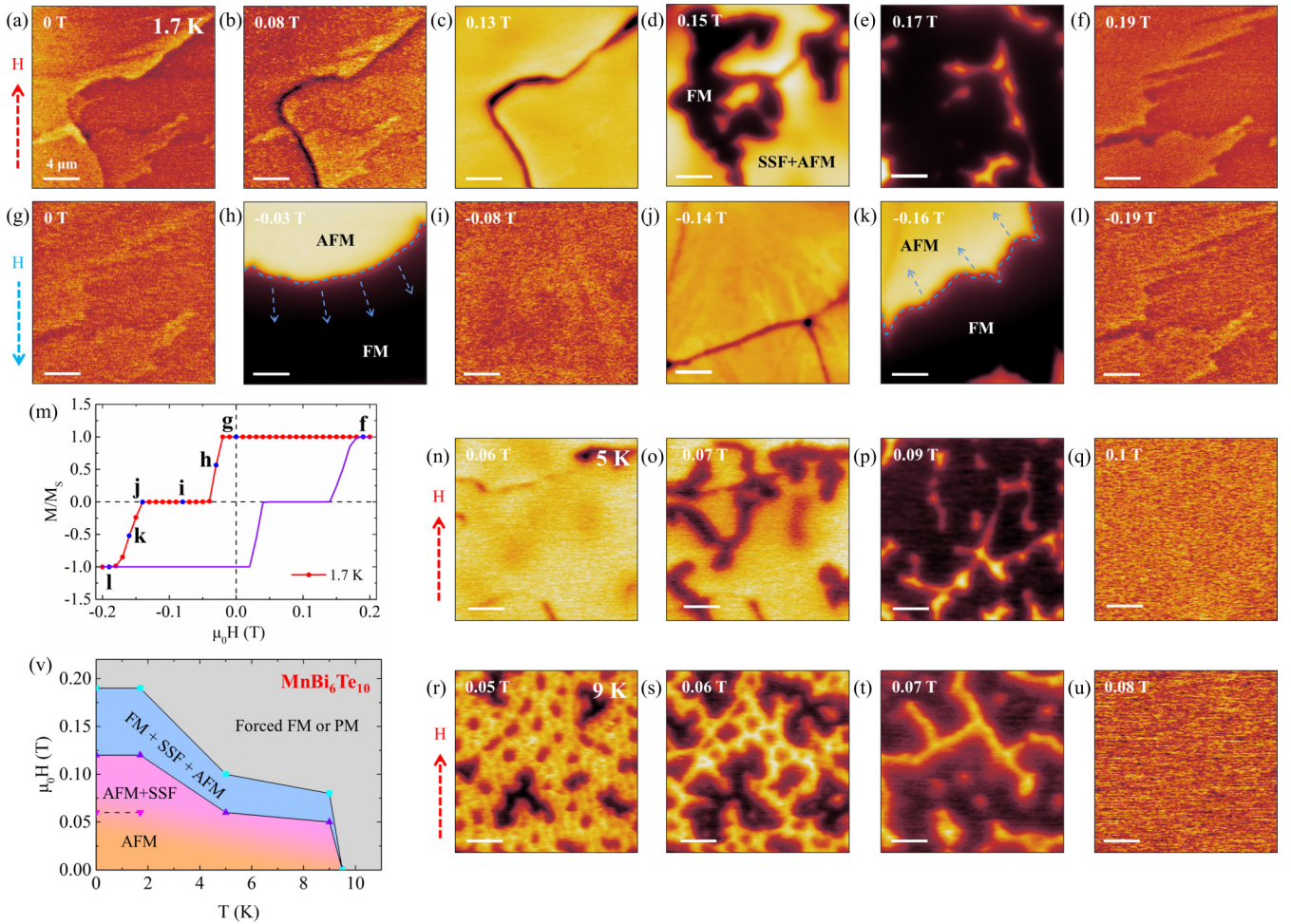


FIG. 3. MFM characterizations of H - and T -dependent magnetic states of $\text{MnBi}_6\text{Te}_{10}$ single crystal. (a)–(l) MFM images of $\text{MnBi}_6\text{Te}_{10}$ at 1.7 K for different magnetic fields. The magnetic field is parallel to c and considered to be positive in the upward direction. (m) M - H hysteresis loop deduced from the H -dependent MFM images of $\text{MnBi}_6\text{Te}_{10}$. The other half (purple line) is replicated from the measurement results via a symmetric operation, assuming that the hysteresis loop is symmetric about the zero field. (n)–(q) MFM images captured at 5 K under increasing magnetic fields. (r)–(u) MFM images captured at 9 K under increasing magnetic fields. (v) H - T phase diagram of $\text{MnBi}_6\text{Te}_{10}$. Scale bar: 4 μm .

bifurcation of ZFC and FC is observed at ~ 10.5 K, indicating an FM transition and consistent with the MFM results [27]. The M - H curves along $H \parallel c$ and $H \parallel ab$ for $\text{MnBi}_6\text{Te}_{10}$ and $\text{MnBi}_8\text{Te}_{13}$ are shown in Figs. 2(j)–2(l) and 2(n)–2(p), respectively. The saturation magnetic moments at 8 T for $\text{MnBi}_6\text{Te}_{10}$ and $\text{MnBi}_8\text{Te}_{13}$ are estimated to be 3.1 and $2.2 \mu_B/\text{Mn}$, respectively, as depicted in Figs. 2(j) and 2(n). For comparison, the saturation magnetic moments of MnBi_2Te_4 and MnBi_4Te_7 near 8 T are determined to be 3.9 and $3.2 \mu_B/\text{Mn}$ [38,32], respectively. All values are smaller than the theoretically predicted saturation value of $4.6 \mu_B/\text{Mn}$, indicating that Mn-Bi site mixing is prevalent in the $\text{MnBi}_2\text{Te}_4(\text{Bi}_2\text{Te}_3)_n$ family [38–41]. It is noteworthy that for $\text{MnBi}_8\text{Te}_{13}$, the remarkably low saturation magnetic moment indicates the presence of an inevitable BT intergrowth.

The detailed inspections of the M - H curves in Figs. 2(l) and 2(p) demonstrate that $\text{MnBi}_6\text{Te}_{10}$ undergoes a spin-flip transition, similar to MnBi_4Te_7 and different from the spin-flop transition of MnBi_2Te_4 , and $\text{MnBi}_8\text{Te}_{13}$ exhibits typical FM hysteresis loop behavior [22]. Upon warming, the increased thermal energy significantly decreased the sat-

uration magnetic fields of $\text{MnBi}_6\text{Te}_{10}$ (A-type AFM) and $\text{MnBi}_8\text{Te}_{13}$ (anisotropic FM). It is noteworthy that although $\text{MnBi}_2\text{Te}_4(\text{Bi}_2\text{Te}_3)_n$ does not show an SLM state at 1.7 K, when the enhanced thermal energy falls in between the interlayer coupling energy (E_{\parallel} , small) and the intralayer coupling energy (E_{\perp} , large), the $\text{MnBi}_2\text{Te}_4(\text{Bi}_2\text{Te}_3)_n$ family could demonstrate some similar magnetic features related to the possible SLM states. In the following, we will focus on the real-space MFM characterizations of $\text{MnBi}_6\text{Te}_{10}$ and $\text{MnBi}_8\text{Te}_{13}$ to investigate their interlayer coupling modulated magnetic properties.

Figures 3(a)–3(f) show typical MFM images of $\text{MnBi}_6\text{Te}_{10}$ with increasing magnetic field (0–0.19 T; Fig. S4). The intrinsic robust A-type AFM phase (0–0.06 T), SSF+AFM phase (0.06–0.13 T), FM+SSF+AFM phase (0.13–0.19 T), and the forced FM phase (>0.19 T) were subsequently realized. The SSF transition occurs first due to the higher susceptibility of the surface magnetic moment to external magnetic fields [Figs. 3(a) and 3(b)] [42]. Then, the FM phase emerges at the domain wall [Fig. 3(c)] and rapidly undergoes expansion [Figs. 3(d) and 3(e)]. At ~ 0.19 T, the entire crystal converts

into the forced FM phase [Fig. 3(f)], and the MBT and BT surface terminations are clearly resolved. Figures 3(g)–3(l) show the MFM images with a decreasing magnetic field (0.19 to -0.19 T) from the forced FM state (Fig. S5). Only until at ~ -0.03 T, the AFM phase appears within the FM phase [Fig. 3(h)] and gradually expands to the whole crystal [Fig. 3(i)]. It is noted that the FM state can be stabilized by itself at 0 T without the additional Zeeman energy. Then, the FM phase reemerges at -0.14 T [Fig. 3(j)], and finally the entire crystal enters the opposite forced FM phase [Fig. 3(l)]. The M - H hysteresis loop can be further deduced from the obtained MFM data, as shown in Fig. 3(m).

To explore signs of the presence of SLM states, we continued with variable temperature MFM measurements. Representative MFM images of $\text{MnBi}_6\text{Te}_{10}$ at 5 K (Fig. S6) and 9 K (Fig. S7) for increasing magnetic fields are shown in Figs. 3(n)–3(q) and 3(r)–3(u), respectively. The saturation field of the sample exhibits a significant decrease with increasing temperature, and the corresponding H - T phase diagram is shown in Fig. 3(v). During the warming process, the evolutionary form of magnetic domains undergoes a transformation at 5 K and becomes more pronounced at 9 K, resulting in the formation of honeycomblike structures. A similar phenomenon was also observed in MnBi_4Te_7 [32]. Considering that both MnBi_4Te_7 and $\text{MnBi}_6\text{Te}_{10}$ are a van der Waals magnet with strong intralayer coupling energy and weak interlayer coupling energy, the interlayer coupling energy is suppressed by thermal energy as the temperature increases. The magnetic behavior of MnBi_4Te_7 and $\text{MnBi}_6\text{Te}_{10}$ is similar at 9 K due to their identical intralayer coupling energy. Therefore, when the temperature increases to the critical temperature, the dominance of intralayer coupling energy in their magnetic properties becomes evident, potentially exhibiting SLM properties. This result is expected to be applicable to all samples exhibiting weak interlayer coupling in the $\text{MnBi}_2\text{Te}_4(\text{Bi}_2\text{Te}_3)_n$ family, suggesting that $\text{MnBi}_8\text{Te}_{13}$ should also exhibit similar magnetic domain behavior as temperature increase. To demonstrate this, we conducted a comprehensive and systematic study into $\text{MnBi}_8\text{Te}_{13}$.

Figures 4(a)–4(f) show typical MFM images obtained on the $\text{MnBi}_8\text{Te}_{13}$ for various magnetic fields (Fig. S8). The MFM image after ZFC exhibits a FM domain structure with an equal distribution of up and down domains [Fig. 4(a)]. As the magnetic field increases, there is no significant expansion of the FM domain region [Fig. 4(b)]. Then, the spin-down domains gradually disappear [Fig. 4(c)]. At ~ 0.09 T, the entire crystal converts into the saturation state [Fig. 4(d)]. The saturation magnetic field of $\text{MnBi}_8\text{Te}_{13}$ is lower than that of $\text{MnBi}_6\text{Te}_{10}$ due to a further reduction in interlayer coupling. For the decreasing magnetic field process, the saturation state exists stably until -0.07 T [Fig. 4(e)], after which the reverse saturation state expands rapidly and occupies the whole crystal at -0.09 T [Fig. 4(f)]. Figure 4(g) shows a histogram of the MFM signal at 0.06 T; spin-up and spin-down regions are identified and marked with their magnetization. A rectangular hysteresis loop can be further deduced from the obtained MFM data, as shown in Fig. 4(h), similar to a uniaxial ferromagnet.

Representative MFM images of $\text{MnBi}_8\text{Te}_{13}$ at 3 K (Fig. S9), 5 K (Fig. S10), 7 K (Fig. S11), and 9 K (Fig.

S12) for decreasing magnetic fields are depicted in Figs. 4(i)–4(x). The saturation field of the sample gradually decreases as the temperature increases, resembling that observed in $\text{MnBi}_6\text{Te}_{10}$. The corresponding H - T phase diagram is shown in Fig. 4(y).

As anticipated, the evolution of magnetic domains in $\text{MnBi}_8\text{Te}_{13}$ also undergoes a transition at 5 K during the warming process. The magnetic domains gradually transform into branching domains and then further develop into honeycomblike domains at 9 K. The similarity in magnetic domain structures observed in MnBi_4Te_7 , $\text{MnBi}_6\text{Te}_{10}$, and $\text{MnBi}_8\text{Te}_{13}$ at 9 K suggests that the influence of interlayer coupling on their magnetic properties diminishes with increasing temperature (Fig. S13). To further verify the above results, we performed zero-field warming MFM measurements on $\text{MnBi}_8\text{Te}_{13}$ in the saturated state (Fig. S14). The whole process can be divided into four distinct stages, wherein similar honeycomblike domains can be observed near phase transition temperature, accompanied by a significant decrease in the MFM signal. This provides additional confirmation that the influence of interlayer coupling on the magnetic properties of $\text{MnBi}_8\text{Te}_{13}$ gradually diminishes with increasing temperature. However, further confirmation is still required through heating to the critical temperature in order to determine whether the $\text{MnBi}_2\text{Te}_4(\text{Bi}_2\text{Te}_3)_n$ family exhibits the SLM state at zero magnetic field. Moreover, considering the specificity of the critical temperature, it may be possible to modulate different topological magnetic structures through the magnetic tip and field, which also needs further study.

In addition, magnetic bubble domain structures are observed in the vicinity of the saturation field of $\text{MnBi}_8\text{Te}_{13}$, commencing at 3 K (Fig. S9). The previous studies have indicated that similar magnetic bubble domains are associated with specific topological effects and may also correspond to the spin configuration of the skyrmion [43–45]. It is noteworthy that the magnetic bubble domain structure is also observed for $\text{MnBi}_6\text{Te}_{10}$ near the phase transition temperature, and it remains to be discussed whether this originates from its interlayer AFM coupling suppressed by thermal fluctuations. Combined with the previously reported light-tunable surface states and half-magnetic topological insulators [30,31], $\text{MnBi}_8\text{Te}_{13}$ is an excellent candidate for the study of novel topological states.

IV. DISCUSSION

A. Intrinsic n -dependent interlayer magnetic coupling

We next discuss the effect of n -dependent interlayer coupling on the magnetic properties of the $\text{MnBi}_2\text{Te}_4(\text{Bi}_2\text{Te}_3)_n$ family. Using the Stoner-Wohlfarth model [46], we can estimate their interlayer coupling J and single-ion (uniaxial) anisotropy D (see details in Supplemental Material Table I). The results demonstrate that the anisotropic energies of the $\text{MnBi}_2\text{Te}_4(\text{Bi}_2\text{Te}_3)_n$ family exhibit similar magnitudes, while the interlayer coupling value decreases by one to two orders of magnitude with increasing BT intercalation layer. The schematic representation of the comparison between J and D is depicted in Figs. 5(a)–5(d).

The combined effects of comparable interlayer coupling energy and anisotropic energy contribute to the distinc-

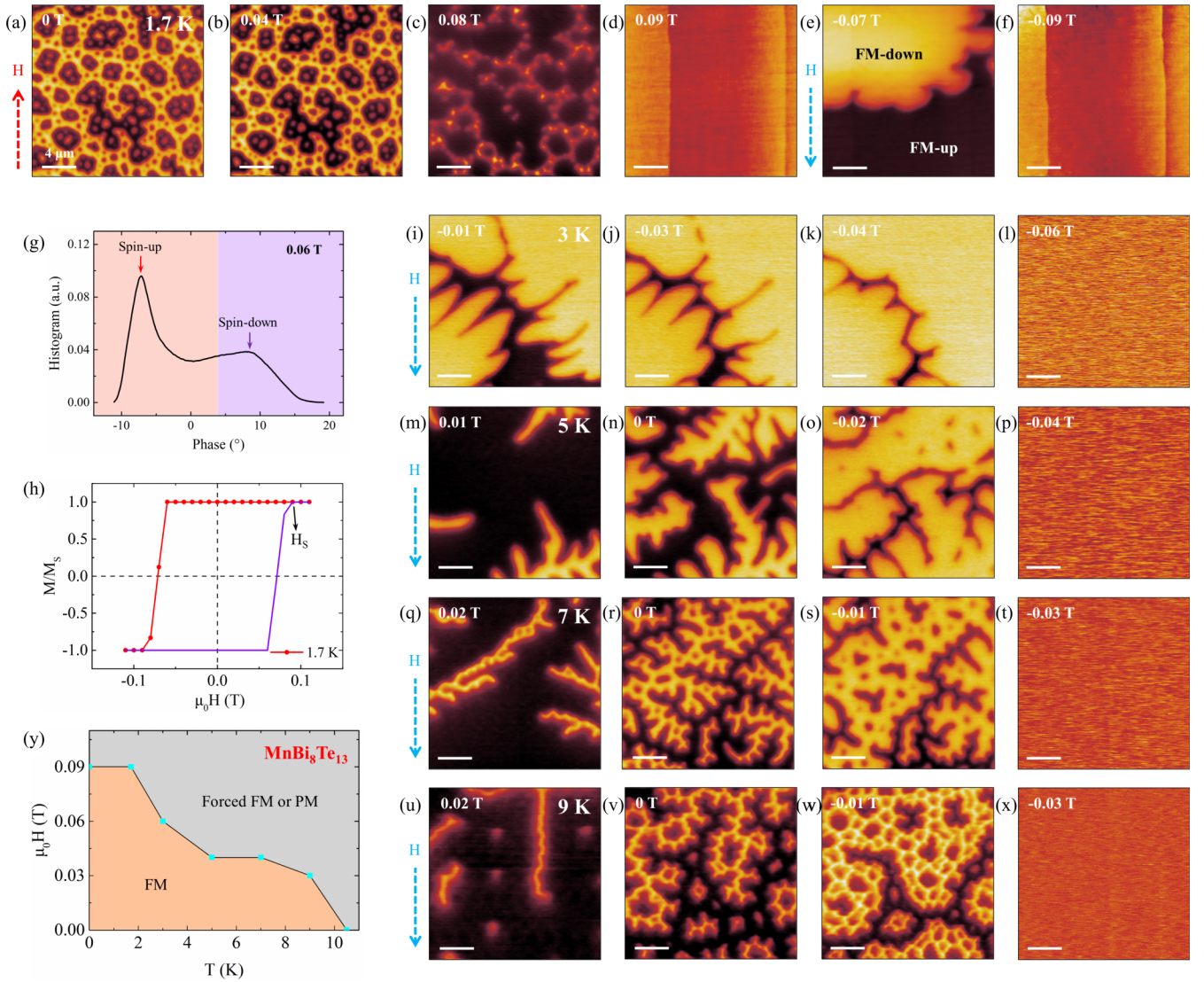


FIG. 4. MFM characterizations of H - and T -dependent magnetic states in $\text{MnBi}_8\text{Te}_{13}$ single crystal. (a)–(f) MFM images of $\text{MnBi}_8\text{Te}_{13}$ at 1.7 K for different magnetic fields. (g) Histogram of the MFM signals for $\text{MnBi}_8\text{Te}_{13}$ at 0.06 T. (h) M - H hysteresis loop deduced from the H -dependent MFM images of $\text{MnBi}_8\text{Te}_{13}$. (i)–(l) MFM images captured at 3 K under increasing magnetic fields. (m)–(p) MFM images captured at 5 K under increasing magnetic fields. (q)–(t) MFM images at 7 K under increasing magnetic fields. (u)–(x) MFM images of $\text{MnBi}_8\text{Te}_{13}$ captured at 9 K under increasing magnetic fields. (y) H - T phase diagram of $\text{MnBi}_8\text{Te}_{13}$. Scale bar: 4 μm .

tive magnetic properties exhibited by MnBi_2Te_4 , as shown in Fig. 5(e) [8]. The strong interlayer coupling induces a spin-flop transition in MnBi_2Te_4 , ultimately reaching saturation at magnetic fields greater than 8 T. In addition, the Néel temperatures (T_N) of MnBi_2Te_4 is 24.5 K, which is higher than the predicted Curie temperature of 12 K for the monolayer MBT, also from the effect of interlayer coupling [15].

The reduction of the interlayer coupling energy leads to a significant change in the magnetic properties of MnBi_4Te_7 and $\text{MnBi}_6\text{Te}_{10}$, as shown in Figs. 5(f) and 5(g) [32]. The weak interlayer coupling results in the transformation of MnBi_4Te_7 ($\text{MnBi}_6\text{Te}_{10}$) into a spin-flip transition, ultimately reaching saturation at 0.22 T (0.19 T). The greater the decoupling between the MBT layers, the closer the magnetic properties of the sample resemble those of a single layer, enabling

stable saturation at 0 T for $\text{MnBi}_6\text{Te}_{10}$. Furthermore, the T_N of MnBi_4Te_7 and $\text{MnBi}_6\text{Te}_{10}$ were significantly reduced to 12.7 and 9.24 K, respectively, similar to the monolayer MBT.

The negligible interlayer coupling energy predicts the disappearance of the interlayer AFM coupling in $\text{MnBi}_8\text{Te}_{13}$, as evidenced by the rectangular hysteresis curve observed in Fig. 5(h). In addition, the magnetic ordering temperature of $\text{MnBi}_8\text{Te}_{13}$ is also similar to monolayer MBT. Therefore, theoretically, the magnetic structure of the $\text{MnBi}_8\text{Te}_{13}$ can be described as a set of decoupled 2D ferromagnets, as shown in Fig. 5(i). The direction within the ab plane exhibits ferromagnetic coupling, while along the c axis, magnetizations in each MBT layer are randomly oriented either parallel or antiparallel to the [001] direction. However, our MFM results indicate that the observed possible features of SLM in

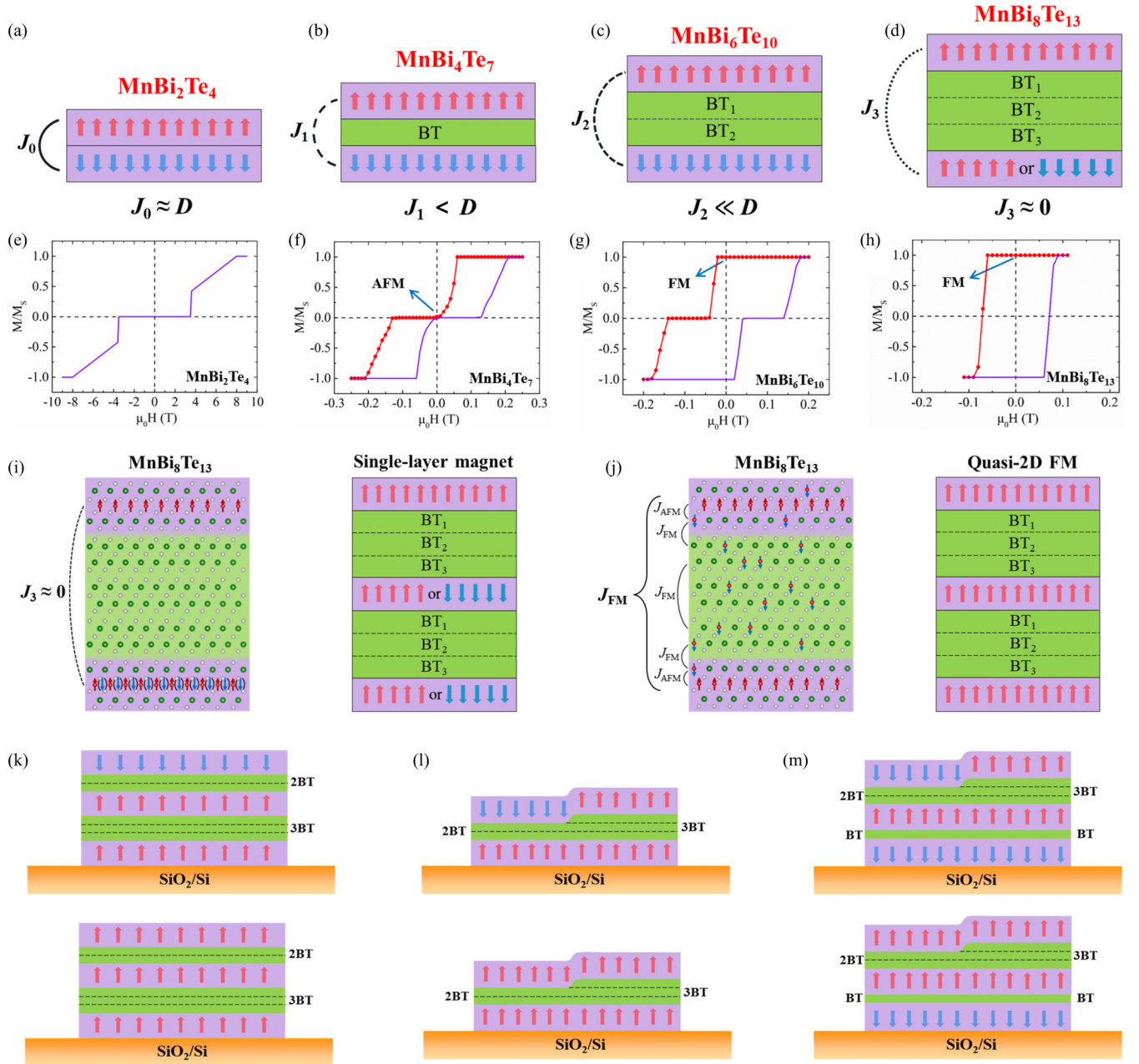


FIG. 5. Schematic diagram of the tunable magnetic ordering state in the $\text{MnBi}_2\text{Te}_4(\text{Bi}_2\text{Te}_3)_n$ multilayers. (a)–(d) Schematic diagram of the intrinsic interlayer coupling modulated magnetic states with increasing BT intercalations. (e) M - H hysteresis of MnBi_2Te_4 . (f)–(h) M - H hysteresis loops of MnBi_4Te_7 (f), $\text{MnBi}_6\text{Te}_{10}$ (g), (c), and $\text{MnBi}_8\text{Te}_{13}$ (h), deduced from the H -dependent MFM images. (i) Schematic diagrams of the intrinsic single-layer magnetic states in $\text{MnBi}_8\text{Te}_{13}$. The zero-field-cooling state of the single-layer magnet demonstrates the intralayer/in-plane FM magnetic ordering and interlayer/out-of-plane PM-like magnetic disordering state. (j) Schematic diagrams of the extrinsic quasi-2D ferromagnetic states in $\text{MnBi}_8\text{Te}_{13}$. The extrinsic FM coupling (J_{FM}) results from the defective-mediated magnetic coupling due to the Mn_{Bi} antisite defects. (k)–(m) Proposed configurable magnetic ordering configurations in the artificial-stacking multilayers for exotic quantum states.

$\text{MnBi}_8\text{Te}_{13}$ are exclusively present at the critical temperature. In contrast, $\text{MnBi}_8\text{Te}_{13}$ exhibits interlayer FM coupling at 1.7 K, which is related to the ubiquitous Mn-Bi site mixing in the $\text{MnBi}_2\text{Te}_4(\text{Bi}_2\text{Te}_3)_n$ family [38,47].

B. Defect-modulated interlayer magnetic coupling

Figure 5(j) shows the schematic diagram of interlayer FM coupling mediated by Mn_{Bi} antisite defects in $\text{MnBi}_8\text{Te}_{13}$.

The Mn atoms occupying Bi positions in both the MBT and the BT layers lead to the emergence of new magnetic couplings. Previous studies have shown that the introduction of Mn_{Bi} antisite defects results in two novel interlayer magnetic exchange interactions: AFM coupling between Mn_{Bi} antisite defects and the main Mn layer (J_4) in the MBT layer and FM coupling between Mn_{Bi} antisite defects in the adjacent MBT (J_5 ; antisite defects in the BT layer can be compatible to J_5) [26,37,48]. Therefore, the interlayer coupling Hamiltonian of

the $\text{MnBi}_8\text{Te}_{13}$ can be written as

$$H_{\perp} = +J \sum_{ij} \mathbf{S}_i^1 \cdot \mathbf{S}_j^2 + J_4 \sum_{ij} \mathbf{S}_i^1 \cdot \mathbf{m}_j^1 \\ + J_4 \sum_{ij} \mathbf{S}_i^2 \cdot \mathbf{m}_j^2 - J_5 \sum_{ij} \mathbf{m}_i^1 \cdot \mathbf{m}_j^2,$$

where \mathbf{S} and \mathbf{m} are the magnetic moments at each Mn and Bi lattice site, and superscripts 1 and 2 represent different MBT layers. Given the negligible coupling between the MBT layers in $\text{MnBi}_8\text{Te}_{13}$, it is the Mn_{Bi} -antisite-defect-mediated coupling that emerges as the primary factor influencing interlayer coupling, thereby facilitating the establishment of an ultralong-range FM order along the c -axis direction (see details in Fig. S15). This Mn_{Bi} -antisite-defect-mediated ultralong-range magnetic ordering disrupts the SLM state of the $\text{MnBi}_8\text{Te}_{13}$. Although the SLM state of $\text{MnBi}_8\text{Te}_{13}$ is replaced by a FM state, SLM can be realized by growing high-quality single crystals. Given the potential resemblance of such SLM to low-dimensional magnets, $\text{MnBi}_8\text{Te}_{13}$ is valuable for both scientific inquiries and technological applications.

We have investigated and obtained interlayer coupling modulated tunable magnetic states in superlattice

$\text{MnBi}_2\text{Te}_4(\text{Bi}_2\text{Te}_3)_n$ topological insulators. Based on the above results, it is promising to design artificial-stacking multilayers with tunable magnetic states to realize exotic quantum states, as shown by some specific configuration in Figs. 5(k)–5(m), including vertical and in-plane heterostructures of different $\text{MnBi}_2\text{Te}_4(\text{Bi}_2\text{Te}_3)_n$. The magnetic state of these stacked multilayers can be finely adjusted by exploiting their interfacial magnetic coupling properties, through the application of a magnetic field. Further experiments are required to investigate the potential application of these artificially stacked multilayers in spintronic devices and for studying topological quantum states.

ACKNOWLEDGMENTS

This project was supported by the Ministry of Science and Technology (MOST) of China (Grants No. 2023YFA1406500 and No. 2019YFA0308602), Strategic Priority Research Program, Chinese Academy of Sciences (CAS; Grant No. XDB30000000), National Natural Science Foundation of China (NSFC; Grants No. 61674045, No. 61911540074, No. 12074425, and No. 11874422), and Fundamental Research Funds for the Central Universities and Research Funds of Renmin University of China (Grants No. 21XNLG27 and No. 22XNH097).

-
- [1] C.-Z. Chang *et al.*, Experimental observation of the quantum anomalous Hall effect in a magnetic topological insulator, *Science* **340**, 167 (2013).
- [2] R. Li, J. Wang, X.-L. Qi, and S.-C. Zhang, Dynamical axion field in topological magnetic insulators, *Nat. Phys.* **6**, 284 (2010).
- [3] Y. Tokura, K. Yasuda, and A. Tsukazaki, Magnetic topological insulators, *Nat. Rev. Phys.* **1**, 126 (2019).
- [4] D. F. Liu, A. J. Liang, E. K. Liu, Q. N. Xu, Y. W. Li, C. Chen, D. Pei, W. J. Shi, S. K. Mo, P. Dudin, T. Kim, C. Cacho, G. Li, Y. Sun, L. X. Yang, Z. K. Liu, S. S. P. Parkin, C. Felser, and Y. L. Chen, Magnetic Weyl semimetal phase in a Kagomé crystal, *Science* **365**, 1282 (2019).
- [5] W. B. Wang, Y. B. Ou, C. Liu, Y. Y. Wang, K. He, Q.-K. Xue, and W. D. Wu, Direct evidence of ferromagnetism in a quantum anomalous Hall system, *Nat. Phys.* **14**, 791 (2018).
- [6] J. Li, Y. Li, S. Du, Z. Wang, B.-L. Gu, S.-C. Zhang, K. He, W. Duan, and Y. Xu, Intrinsic magnetic topological insulators in van der Waals layered MnBi_2Te_4 -family materials, *Sci. Adv.* **5**, eaaw5685 (2019).
- [7] J.-Q. Yan, Q. Zhang, T. Heitmann, Z. Huang, K. Y. Chen, J.-G. Cheng, W. Wu, D. Vaknin, B. C. Sales, and R. J. McQueeney, Crystal growth and magnetic structure of MnBi_2Te_4 , *Phys. Rev. Mater.* **3**, 064202 (2019).
- [8] M. M. Otrokov *et al.*, Prediction and observation of an antiferromagnetic topological insulator, *Nature (London)* **576**, 416 (2019).
- [9] D. Zhang, M. Shi, T. Zhu, D. Xing, H. Zhang, and J. Wang, Topological axion states in the magnetic insulator MnBi_2Te_4 with the quantized magnetoelectric effect, *Phys. Rev. Lett.* **122**, 206401 (2019).
- [10] Y. Deng, Y. Yu, M. Z. Shi, Z. Guo, Z. Xu, J. Wang, X. H. Chen, and Y. Zhang, Quantum anomalous Hall effect in intrinsic magnetic topological insulator MnBi_2Te_4 , *Science* **367**, 895 (2020).
- [11] C. Liu, Y. Wang, H. Li, Y. Wu, Y. Li, J. Li, K. He, Y. Xu, J. Zhang, and Y. Wang, Robust axion insulator and Chern insulator phases in a two-dimensional antiferromagnetic topological insulator, *Nat. Mater.* **19**, 522 (2020).
- [12] J. Ge, Y. Z. Liu, J. H. Li, H. Li, T. C. Luo, Y. Wu, Y. Xu, and J. Wang, High-Chern-number and high-temperature quantum Hall effect without Landau levels, *Natl. Sci. Rev.* **7**, 1280 (2020).
- [13] S. Q. Yang, X. L. Xu, Y. Z. Zhu, R. R. Niu, C. Q. Xu, Y. X. Peng, X. Cheng, X. H. Jia, Y. Huang, X. F. Xu, J. M. Lu, and Y. Ye, Odd-even layer-number effect and layer-dependent magnetic phase diagrams in MnBi_2Te_4 , *Phys. Rev. X* **11**, 011003 (2021).
- [14] D. Ovchinnikov, X. Huang, Z. Lin, Z. Fei, J. Cai, T. Song, M. He, Q. Jiang, C. Wang, H. Li, Y. Wang, Y. Wu, D. Xiao, J.-H. Chu, J. Yan, C.-Z. Chang, Y.-T. Cui, and X. Xu, Intertwined topological and magnetic orders in atomically thin Chern insulator MnBi_2Te_4 , *Nano Lett.* **21**, 2544 (2021).
- [15] M. M. Otrokov, I. P. Rusinov, M. Blanco-Rey, M. Hoffmann, A. Y. Vyazovskaya, S. V. Ereemeev, A. Ernst, P. M. Echenique, A. Arnau, and E. V. Chulkov, Unique thickness-dependent properties of the van der Waals interlayer antiferromagnet MnBi_2Te_4 films, *Phys. Rev. Lett.* **122**, 107202 (2019).
- [16] K. Volckaert, P. Majchrzak, D. Biswas, A. J. H. Jones, M. Bianchi, Z. Jiang, R. Dubourg, R. Ø. Stenshøj, M. L. Jensen, N. C. Jones, S. V. Hoffmann, J.-L. Mi, M. Bremholm, X.-C. Pan, Y. P. Chen, P. Hofmann, J. A. Miwa, and S. Ulstrup, Surface electronic structure engineering of manganese bismuth tellurides guided by micro-focused angle-resolved photoemission, *Adv. Mater.* **35**, 2301907 (2023).

- [17] H. Padmanabhan *et al.*, Large exchange coupling between localized spins and topological bands in MnBi_2Te_4 , *Adv. Mater.* **34**, 2202841 (2022).
- [18] A. R. Mazza, J. Lapano, H. M. Meyer, C. T. Nelson, T. Smith, Y.-Y. Pai, K. Noordhoek, B. J. Lawrie, T. R. Charlton, R. G. Moore, T. Z. Ward, M.-H. Du, G. Eres, and M. Brahlek, Surface-driven evolution of the anomalous Hall effect in magnetic topological insulator MnBi_2Te_4 thin films, *Adv. Funct. Mater.* **32**, 2202234 (2022).
- [19] P. M. Sass, W. Ge, J. Yan, D. Obeysekera, J. J. Yang, and W. Wu, Magnetic imaging of domain walls in the antiferromagnetic topological insulator MnBi_2Te_4 , *Nano Lett.* **20**, 2609 (2020).
- [20] P. M. Sass, J. Kim, D. Vanderbilt, J. Yan, and W. Wu, Robust A-type order and spin-flop transition on the surface of the antiferromagnetic topological insulator MnBi_2Te_4 , *Phys. Rev. Lett.* **125**, 037201 (2020).
- [21] Z. S. Aliev, I. R. Amirasanov, D. I. Nasonova, A. V. Shevelkov, N. A. Abdullayev, Z. A. Jahangirli, E. N. Orujlu, M. M. Otrokov, N. T. Mamedov, M. B. Babanly, and E. V. Chulkov, Novel ternary layered manganese bismuth tellurides of the $\text{MnTe-Bi}_2\text{Te}_3$ system: Synthesis and crystal structure, *J. Alloys Compd.* **789**, 443 (2019).
- [22] I. I. Klimovskikh *et al.*, Tunable 3D/2D magnetism in the $(\text{MnBi}_2\text{Te}_4)(\text{Bi}_2\text{Te}_3)_m$ topological insulators family, *npj Quantum Mater.* **5**, 54 (2020).
- [23] J. Wu, F. Liu, C. Liu, Y. Wang, C. Li, Y. Lu, S. Matsuishi, and H. Hosono, Toward 2D magnets in the $(\text{MnBi}_2\text{Te}_4)(\text{Bi}_2\text{Te}_3)_n$ bulk crystal, *Adv. Mater.* **32**, 2001815 (2020).
- [24] C. Hu, K. N. Gordon, P. Liu, J. Liu, X. Zhou, P. Hao, D. Narayan, E. Emmanouilidou, H. Sun, Y. Liu, H. Brawer, A. P. Ramirez, L. Ding, H. Cao, Q. Liu, D. Dessau, and N. Ni, A van der Waals antiferromagnetic topological insulator with weak interlayer magnetic coupling, *Nat. Commun.* **11**, 97 (2020).
- [25] A. Tan, V. Labracherie, N. Kunchur, A. U. B. Wolter, J. Cornejo, J. Dufouleur, B. Büchner, A. Isaeva, and R. Giraud, Metamagnetism of weakly coupled antiferromagnetic topological insulators, *Phys. Rev. Lett.* **124**, 197201 (2020).
- [26] X. L. Xu, S. Q. Yang, H. Wang, R. Guzman, Y. C. Gao, Y. Z. Zhu, Y. X. Peng, Z. H. Zang, M. Xi, S. J. Tian, Y. P. Li, H. C. Lei, Z. C. Luo, J. B. Yang, Y. L. Wang, T. L. Xia, W. Zhou, Y. Huang, and Y. Ye, Ferromagnetic-antiferromagnetic coexisting ground state and exchange bias effects in MnBi_4Te_7 and $\text{MnBi}_6\text{Te}_{10}$, *Nat. Commun.* **13**, 7646 (2022).
- [27] C. Hu *et al.*, Realization of an intrinsic ferromagnetic topological state in $\text{MnBi}_8\text{Te}_{13}$, *Sci. Adv.* **6**, eaba4275 (2020).
- [28] L. Ding, C. Hu, E. Feng, C. Jiang, I. A. Kibalin, A. Gukasov, M. Chi, N. Ni, and H. Cao, Neutron diffraction study of magnetism in van der Waals layered $\text{MnBi}_{2n}\text{Te}_{3n+1}$, *J. Phys. D: Appl. Phys.* **54**, 174003 (2021).
- [29] C. Hu, M. A. Tanatar, R. Prozorov, and N. Ni, Unusual dynamic susceptibility arising from soft ferromagnetic domains in $\text{MnBi}_8\text{Te}_{13}$ and Sb-doped $\text{MnBi}_{2n}\text{Te}_{3n+1}$ ($n = 2, 3$), *J. Phys. D: Appl. Phys.* **55**, 054003 (2022).
- [30] H. Zhong, C. Bao, H. Wang, J. Li, Z. Yin, Y. Xu, W. Duan, T.-L. Xia, and S. Zhou, Light-tunable surface state and hybridization gap in magnetic topological insulator $\text{MnBi}_8\text{Te}_{13}$, *Nano Lett.* **21**, 6080 (2021).
- [31] R. Lu *et al.*, Half-magnetic topological insulator with magnetization-induced Dirac gap at a selected surface, *Phys. Rev. X* **11**, 011039 (2021).
- [32] J. F. Guo, H. Wang, X. Y. Wang, S. Z. Gu, S. Mi, S. Y. Zhu, J. W. Hu, F. Pang, W. Ji, H.-J. Gao, T. L. Xia, and Z. H. Cheng, Coexisting ferromagnetic-antiferromagnetic phases and manipulation in a magnetic topological insulator MnBi_4Te_7 , *J. Phys. Chem. C* **126**, 13884 (2022).
- [33] W. B. Ge, J. Kim, Y.-T. Chan, D. Vanderbilt, J. Q. Yan, and W. Wu, Direct visualization of surface spin-flip transition in MnBi_4Te_7 , *Phys. Rev. Lett.* **129**, 107204 (2022).
- [34] S. Mi, J. F. Guo, H. Wang, T. L. Xia, and Z. H. Cheng, Scanning Kelvin probe microscopy study of magnetic topological insulators $\text{MnBi}_2\text{Te}_4(\text{Bi}_2\text{Te}_3)_n$, *Chin. J. Vac. Sci. Technol.* **42**, 585 (2022).
- [35] See Supplemental Material at <http://link.aps.org/supplemental/10.1103/PhysRevB.109.165410> for more details about theoretical calculation, SKPM and MFM data.
- [36] G. Akhgar, Q. L. Li, I. D. Bernardo, C. X. Trang, C. Liu, A. Zavabeti, J. Karel, A. Tadich, M. S. Fuhrer, and M. T. Edmonds, Formation of a stable surface oxide in MnBi_2Te_4 thin films, *ACS Appl. Mater. Interfaces* **14**, 6102 (2022).
- [37] D. Haneman, Photoelectric emission and work functions of InSb, GaAs, Bi_2Te_3 and germanium, *J. Phys. Chem. Solids* **11**, 205 (1959).
- [38] Y. Lai, L. Ke, J. Yan, R. D. McDonald, and R. J. McQueeney, Defect-driven ferrimagnetism and hidden magnetization in MnBi_2Te_4 , *Phys. Rev. B* **103**, 184429 (2021).
- [39] Y. Liu, L.-L. Wang, Q. Zheng, Z. Huang, X. Wang, M. Chi, Y. Wu, B. C. Chakoumakos, M. A. McGuire, B. C. Sales, W. Wu, and J. Yan, Site mixing for engineering magnetic topological insulators, *Phys. Rev. X* **11**, 021033 (2021).
- [40] M.-H. Du, J. Q. Yan, V. R. Cooper, and M. Eisenbach, Tuning Fermi levels in intrinsic antiferromagnetic topological insulators MnBi_2Te_4 and MnBi_4Te_7 by defect engineering and chemical doping, *Adv. Funct. Mater.* **31**, 2006516 (2021).
- [41] A.-V. Tcakaev *et al.*, Intermixing-driven surface and bulk ferromagnetism in the quantum anomalous Hall candidate $\text{MnBi}_6\text{Te}_{10}$, *Adv. Sci.* **10**, 2203239 (2023).
- [42] U. K. Rößler and A. N. Bogdanov, Reorientation in antiferromagnetic multilayers: Spin-flop transition and surface effects, *Phys. Status Solidi C* **1**, 3297 (2004).
- [43] L. Vistoli, W. B. Wang, A. Sander, Q. X. Zhu, B. Casals, R. Cichelero, A. Barthélémy, S. Fusil, G. Herranz, S. Valencia, R. Abrudan, E. Weschke, K. Nakazawa, H. Kohno, J. Santamaria, W. Wu, V. Garcia, and M. Bibes, Giant topological Hall effect in correlated oxide thin films, *Nat. Phys.* **15**, 67 (2019).
- [44] C. Feng, F. Meng, Y. Wang, J. Jiang, N. Mehmood, Y. Cao, X. Lv, F. Yang, L. Wang, Y. Zhao, S. Xie, Z. Hou, W. Mi, Y. Peng, K. Wang, X. Gao, G. Yu, and J. Liu, Field-free manipulation of skyrmion creation and annihilation by tunable strain engineering, *Adv. Funct. Mater.* **31**, 2008715 (2021).
- [45] Y. Wu, B. Francisco, Z. Chen, W. Wang, Y. Zhang, C. Wan, X. Han, H. Chi, Y. Hou, A. Lodesani, G. Yin, K. Liu, Y.-T. Cui, K. L. Wang, and J. S. Moodera, A Van der Waals interface hosting two groups of magnetic skyrmions, *Adv. Mater.* **34**, 2110583 (2022).
- [46] E. C. Stoner and E. Wohlfarth, A mechanism of magnetic hysteresis in heterogeneous alloys, *Philos. Trans. R. Soc. A* **240**, 599 (1948).

- [47] F. Islam, Y. Lee, D. M. Pajerowski, J. Oh, W. Tian, L. Zhou, J. Yan, L. Ke, R. J. McQueeney, and D. Vaknin, Role of magnetic defects in tuning ground states of magnetic topological insulators, *Adv. Mater.* **35**, 2209951 (2023).
- [48] J. Henk, M. Flieger, I. V. Maznichenko, I. Mertig, A. Ernst, S. V. Ereemeev, and E. V. Chulkov, Topological character and magnetism of the Dirac state in Mn-Doped Bi₂Te₃, *Phys. Rev. Lett.* **109**, 076801 (2012).